AIAA SciTech Forum
January 3-7, 2022, San Diego, CA & Virtual
AIAA SCITECH 2022 Forum

10.2514/6.2022-1795



# Low-Wavenumber Wall Pressure Measurements in Zero-Pressure Gradient Boundary Layer Flow

Shishir Damani*, Humza Butt*, Jarrod Banks*, Surabhi Srivastava*, Agastya Balantrapu‡, Todd Lowe††, and William J. Devenport§
*Virginia Polytechnic Institute and State University, Blacksburg Virginia 24060, United States of America*

**Low-wavenumber pressure fluctuations generated by turbulent boundary layers are the source of both flow-generated sound and structural vibration in many applications. However, the form and origin of these fluctuations are poorly understood, not least because measurement of this component of the wall pressure spectrum is especially challenging. This paper describes a new method for low-wavenumber pressure measurement using arrays of resonating sensors inspired by acoustic metamaterials. Measurements are made using the array in high Reynolds number turbulent boundary layers and show the sub-convective components of the wall pressure spectrum in a zero-pressure gradient turbulent boundary layer flow.**

## I. Introduction

Turbulent pressure fluctuations on aerodynamic surfaces generate sound by exciting vibrations of the aerodynamic surface itself or by scattering at salient geometric features, such as a trailing edge. The wavenumber frequency spectrum of wall pressure $\Phi_{pp}(\boldsymbol{k},\omega)$ is the simplest time-averaged form of the pressure fluctuation field that has sufficient sophistication to represent the acoustic or vibration source. There have been a number of studies on prediction models of the wavenumber spectrum for an equilibrium two-dimensional turbulent boundary layer over a planar surface. These models typically have considerable uncertainty in their predictions at wavenumbers below the

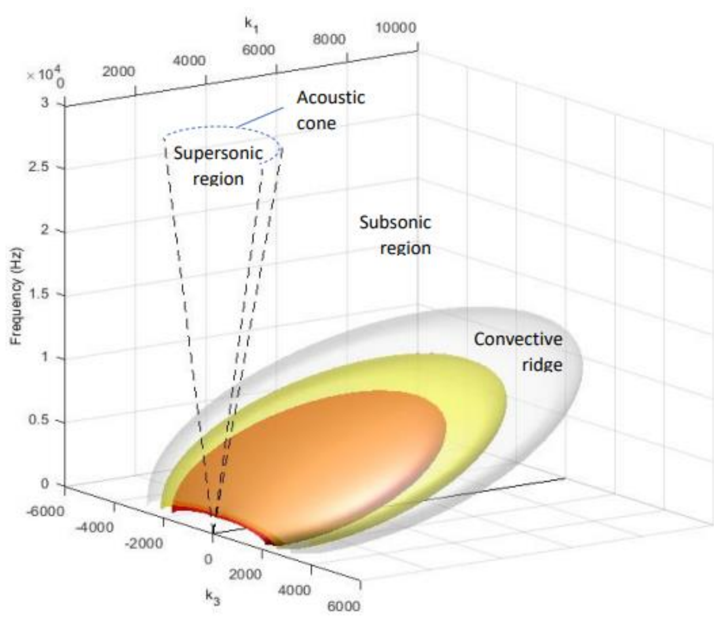


**Figure 1:** Schematic of the wall-pressure wavevector frequency spectrum

---

*Ph.D. Student, Kevin T. Crofton Department of Aerospace and Ocean Engineering.
‡Research Associate, Kevin T. Crofton Department of Aerospace and Ocean Engineering.
††Associate Professor, Kevin T. Crofton Department of Aerospace and Ocean Engineering. Senior Member AIAA.
§Professor, Kevin T. Crofton Department of Aerospace and Ocean Engineering. Associate Fellow AIAA.

convective ridge because of a lack of experimental verification. Models of the wall pressure wavenumber frequency spectrum are reviewed by Blake [1], Graham [2], Liu and Dowling [3], and Juve [4] amongst others. The models themselves include the widely used Corcos model [5], which uses a simple separation of variables approach and early measurements made by Bull [6] and Willmarth and Woolridge [7] that indicated that decaying exponentials could be used to represent variations seen in the convective ridge. The Chase model [8, 9], made particularly accessible in the description of Blake [1], is generally regarded as the most accurate model. It was derived directly using the Poisson equation, and arguments about the possible form of the mean shear turbulence and turbulence-turbulence correlation terms. Other models include those due to Efimtsov (which extends Corcos' approach), Smol'yakov and Tkachenko, and Ffowcs Williams, see [1-3].

Figure 1 depicts the general form of the wavenumber frequency spectrum for a low Mach number turbulent boundary layer. Pressure fluctuations produced directly by the footprint of the turbulent eddies are primarily found in the convective ridge with a slope (in streamwise wavenumber $k_1$ and frequency) roughly equal to the average convection speed of the eddies, typically between 60 and 80% of the boundary layer edge velocity. The boundary layer also produces weak pressure fluctuations at wavenumber frequency combinations away from the convective ridge associated, presumably, with elongated turbulent structures, non-sinusoidal components of convected eddies, near-field sound waves generated within the turbulence and scattered from any non-planar features of the surface. Sound waves grazing the surface appear on an acoustic cone with a surface slope equal to the sound speed, and all other sound waves appear within the cone because of their supersonic trace velocity across the wall. This is called the supersonic region of the spectrum. This and the subsonic region, between the acoustic cone and the convective ridge, are the most important regions for coupling to vibration modes of an elastic wall or the acoustic far-field via a scattering edge.

There appear to be at least three techniques that have been attempted for separating these components of the pressure field from the much more intense fluctuations associated with the convective ridge. Using a regularly spaced array (linear or rectangular) of large area pressure fluctuation sensors was an approach pioneered by Maidanik [10, 11] and further developed and applied by Blake and Chase [12, 13], Farabee and Geib [14] and Kudashev [15], among others. An example of this 'small array/large sensor' approach are the measurements of Farabee and Geib made of the low-wavenumber components of turbulent boundary layers just downstream of roughness fetches. Measurements were made using six 1-inch B&K microphones spaced at intervals of $d = 26.9\ mm$ in a linear streamwise array. By differencing alternate microphone outputs, the array was used to discriminate pressure fluctuations around $k_1 = \pi/d$. By selecting suitable frequencies ($6\ kHz$ and $2.5\ kHz$) this difference mode array was then used to infer spectral levels in the sonic and subsonic regions. The regular structure of the array enabled these simple manipulations, practical in the analog electronic systems of the time, to yield measurements at specific wavenumbers. The large area of the sensors served to filter out much of the unwanted pressure fluctuations associated with convective ridge motions, but some portion of these work to confound the measurement through spatial aliasing. Aliasing seems inevitable in any array with a sensor spacing that fails to resolve the smallest turbulent scales - the sensor diameter needed to anti-alias filter the pressure field through area averaging is at least twice the sensor spacing, implying overlapping sensors. A much finer regular linear array of some 48, $3\ mm$ diameter pressure sensors was used by Abraham and Keith [16] to try to alleviate this issue. Likewise, Manoha [17] used an evenly spaced linear array of some $32, 8.3\ mm$ diameter hydrophones, and Bremner [18] used a similar array of MEMS microphones on a flexible substrate to study the space-time correlation structure of the flow over a car side window in the wake of a wing mirror. The larger number of sensors used in both these studies and the more modern measurement technologies available allowed for direct spatial Fourier transforming of the measurements.

A second method used in the measurement of the low wavenumber components of the wall pressure spectrum is to use a thin flexible membrane excited by these large-scale motions. Representative studies are Martin and Leehey [19], who studied a Mylar membrane excited by a plane wall boundary layer in air, Bonness [20] who used a thin cylindrical aluminum shell carrying a turbulent pipe flow, and Golubev [21] who studied thin aluminum alloy and glass plates deflected under a planar turbulent boundary layer. Bonness [20] studied turbulent flow through a $1.22\ m$ long, $150\ mm$ diameter pipe instrumented with accelerometers. The raw measurements revealed the resonant response of the structural modes in the pipe wall, which are then related to the modal force (using experimentally determined mode shapes), which in turn is related to the wavenumber spectrum of the wall pressure fluctuations providing the excitation. The analysis process requires iterative adjustment of the wavenumber spectrum level until the experimentally measured vibration levels are matched. A comparison of these studies with the Chase model has been shown in Figure 2. The small peaks in the model results coincide with the acoustic cone, and the large peak with the convective ridge. Note that the model predictions are shown for a Mach number representative of hydrodynamic applications ($0.004$). For low speed aeroacoustic applications the scale separation between the acoustic cone and convective ridge would be at least an order of magnitude smaller. Agreement between model and measurements appears reasonable in the subsonic range, but even here the overall uncertainty in levels appears to be on the order of $10\ dB$. This uncertainty is too great for sufficiently accurate sound and vibration predictions. Panel vibration measurements have produced some of the lowest wavenumber measurements of the surface pressure spectrum (several orders of magnitude below the convective wavenumber). The method, however, appears less easily adapted than sensor-based approaches to inhomogeneous boundary layer studies.

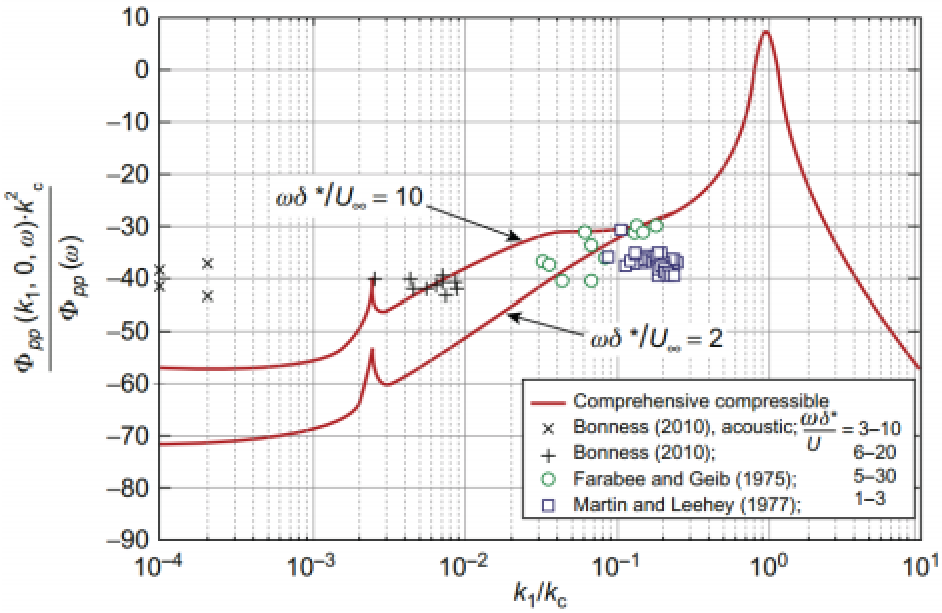


**Figure 2:** Comparison of wall pressure wavenumber frequency spectrum measurements with Chase model predictions (Blake [1]).

A third approach for wavenumber-frequency spectrum measurement has been to use large arrays of electret, remote or digital microphones that can resolve some of the smaller turbulent scales. This has been a particular focus of researchers interested in automobile wind noise, specifically interior noise generated by pressure fluctuations on car side windows enhanced by the presence of the upstream A-frame pillar and wing mirror. A sequence of studies using this approach was initiated at Ecole Centrale de Lyon by Arguillat [23]. They used 63 microphones mounted in array across the diameter of an "antenna" disk, embedded in a wall under a turbulent boundary layer, that could be rotated to different angular positions. The goal of this type of measurement is to measure the spatial dependence of the two-point cross-spectrum of wall pressure fluctuations as fully as possible, which can then be Fourier transformed to yield the wavenumber frequency spectrum of wall pressure. This study and its successors [24-28] have used this approach to reveal elements of the three-dimensional wavenumber frequency spectra of two-dimensional turbulent boundary layers subject to zero, favorable and adverse pressure gradients. Ehrenfield and Koop [29] demonstrated in 2005 that estimates of wavenumber frequency spectra from surface pressure array data could be deconvolved using procedures similar to those developed for beamforming with far-field acoustic arrays.

Ehrenfield and Koop [29], along with a number of others, also realized that for homogeneous pressure fields only the sensor separation vector is important in determining the two-point surface pressure characteristics. Regular arrays of sensors have many repetitions of the same separation and so can be considerably less effective in defining a large range of scales than arrays designed to optimize the number and distribution of separation vectors, the so-called co-array. Using this approach, they designed a $0.6\ m$ square array of some $48$ point pressure sensors for measuring the wavenumber frequency spectrum of a zero-pressure gradient turbulent boundary layer. Gabriel [30] also employed this approach to study the space-time correlation structure of the flow over a car side window in the wake of a wing mirror. Arrays of $92$ digital MEMS microphones were mounted in a $52\ mm$ wide single array designed to define

1849 distinct separation vectors. Measurements were processed to obtain wavenumber spectra assuming local homogeneity. Most recently Schram [31] used an optimization scheme to place 64 electret microphones on a rotatable disk so as to define a detailed and effective co-array. Measurements made in a zero pressure gradient turbulent boundary layer appear quite similar to those of Prigent [27, 28], Arguillat [23, 24] and Ehrenfield and Koop [29]. Specifically, investigators using this large array/small sensor approach have been able to produce maps that clearly reveal the convective ridge and acoustic cone. However, it is not at all clear that this strategy is capable of revealing the low spectral levels associated with the boundary layer in the subsonic region away from the convective ridge.

In summary, low-wavenumber measurements in homogeneous boundary layers have previously been attempted using large sensor/small array, small sensor/large array, and flexible membrane methods. While the membrane approach has supplied important data for homogeneous boundary layers, it does not appear suitable for the inhomogeneous problem. The large sensor/small array method has the advantage of sensors that inherently filter out a significant portion of contaminating convective pressure fluctuations but appears to suffer from inherent spatial aliasing. The small sensor/large array approach suffers less from aliasing since it resolves the convective pressures, but then appears to be frustrated by complementary problems of signal to noise ratio in resolving the sub-convective domain. This paper describes a new method for low-wavenumber pressure measurement using arrays of resonating sensors inspired by acoustic metamaterials. A brief description of the sensor is made here along with results proving the averaging behavior of the sensor which makes the use of the sensor viable for this application. The approach allows for flexibility in geometry that then allows for the design of arrays that reduce much of the aliasing experienced in previous work using small arrays of large sensors. We have used this new array to make measurements in a series of high Reynolds number canonical turbulent boundary layers, with well documented mean-flow, turbulence, and convective wall pressure properties [33, 34]. In this paper we describe the array as well as PIV instrumentation used to provide accompanying information about the boundary layer turbulence structure with zero-pressure gradient.

## II. Experimental Facility and Instrumentation

### A. Virginia Tech Stability Wind Tunnel

This experimental study was conducted in the Virginia Tech Stability Wind Tunnel (SWT), as shown in Figure 2. It is a closed-circuit, single return, subsonic wind tunnel with a test section which can be configured with Kevlar side walls, or aluminum panel sidewalls to permit different acoustic and aerodynamic configurations. The test section is $7.32\ m$ long and $1.83 \times 1.83\ m$ in cross section. The SWT can support a maximum flow speed of $80\ ms^{-1}$ which corresponds to a Reynolds number of about 5 million per meter. The experiments in this study were conducted with aluminum side walls. This configuration comprises of $2' \times 2'$ square panels, arranged in a grid pattern which can be removed and replaced with custom instrumentation [34]. The floor and the ceiling of the SWT were also lined with

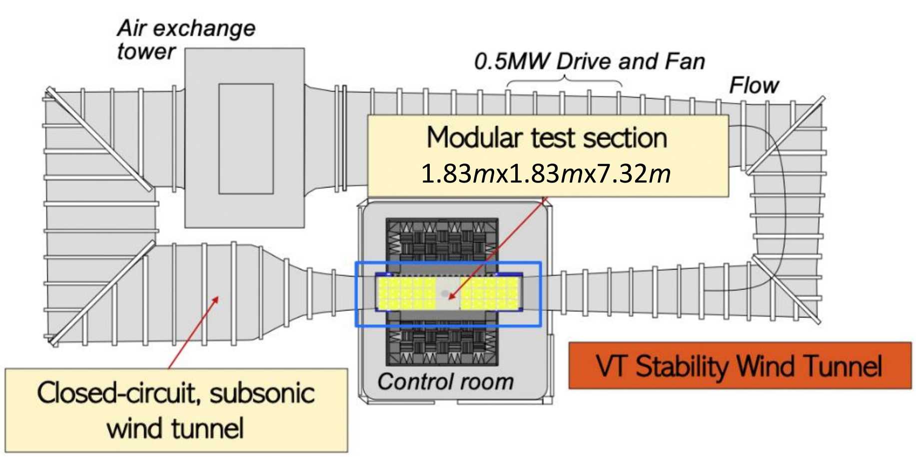


**Figure 3:** General layout of the VT Stability Wind Tunnel

foam wedges to minimize ambient noise pollution from the surroundings of the facility. The free-stream turbulence of the SWT is documented to be quite low, at about 0.012 % at 20 $m/s$ and increasing gradually to about 0.031% at 57 $ms^{-1}$.

A top-down view of the test section is presented in Figure 4. The flow enters the contraction, prior to the test section where it is tripped using a 3.18 $mm$ thick trip strip to transition into fully turbulent flow once it reaches the test section (shown in Figure 4). The test section houses a 0.91 $m$ chord NACA 0012 airfoil mounted on a turntable for changing angle of attacks to achieve a wide range of pressure gradients, both adverse and favorable, on the boundary layer of the test-section walls. The airfoil quarter chord is positioned, nominally, at $x = 3.43\,m$ and $y = 0.925\,m$. Throughout this paper, the two side walls of the test section will be referred to as either the "port" wall or the "starboard" wall, which respectively correspond to the walls facing the pressure and suction side of the airfoil (marked in Figure 4). All panels of the test section have static pressure taps running along the center line in the flow direction, which are used to derive the pressure gradient impressed by the airfoil on the walls. The mean pressure distribution on the airfoil and the corresponding pressure distribution imposed on the walls were measured as a function of the angle of attack of the airfoil and Reynolds number. The pressure distribution was measured via 0.5 $mm$ holes tapped on the surface/walls with flexible Tygon tubes connected to a combination of DTC Initium ESP-32HD acquisition system (range = 10 in. WC and accuracy = ±0.05%) as wells as an Esterline 98RK-1 NetScaner system (range = 2.5 PSI and accuracy = 0.05%).

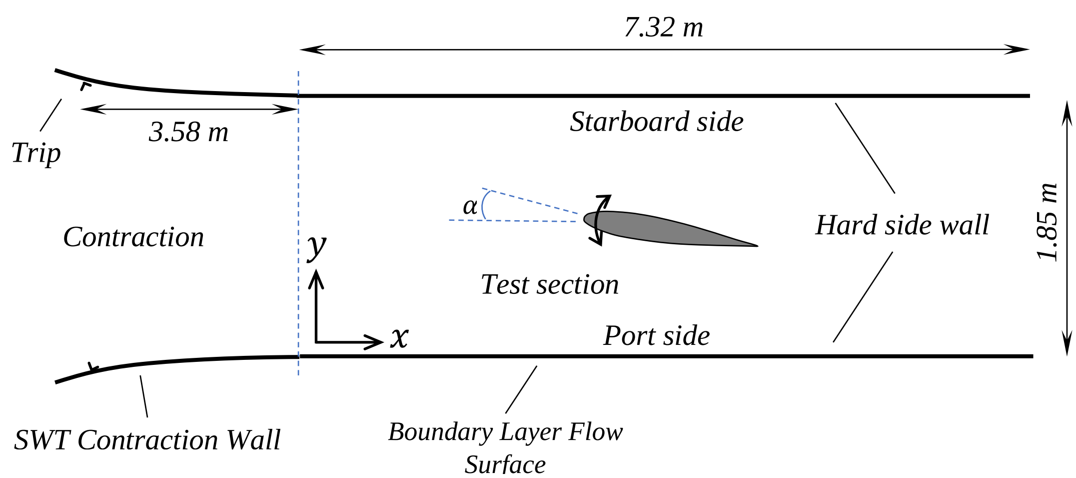


**Figure 4:** Top-down view of the test section of the Stability Wind Tunnel at Virginia Tech

### B. Velocity and turbulence Measurements

Measurements of the mean flow and turbulence in the boundary layer were made with a combination of a Pitot-probe rake and time-resolved Particle Image Velocimetry (PIV). The Pitot-probe rake device comprised of 30 pitot-static probes spaced with increasing separation. To minimize the aerodynamic blockage and unsteady flow separation, this rake was installed within a NACA 0012 profile fairing. The fairing had a chord length of 114 $mm$ and a total span of 191 $mm$. The probes were extruded upstream, to a distance of 101 $mm$ from the leading edge of the aerodynamic fairing and were installed in a logarithmic fashion to measure the stagnation pressure of the flow at 30 instances normal to the wall. The probes spanned from $y = 1$ to 178 $mm$ normal to the wall. Figure 5 shows the Boundary Layer Rake during one of the experiments on the port wall of the Stability Wind Tunnel. The static pressure was measured using the static pressure ports on the panel, just below the stagnation point of the rake. The pressure data collected from the rake was sampled using DTC ESP 32HD 20" water pressure scanner. Boundary layer rake measurements were made at various streamwise points along the centerline of the port wall of the Stability Wind Tunnel. The Clauser plot method [35] was used to estimate the wall shear stresses using the boundary layer rake data, where Spalding [36] profile was used instead of the piecewise law of the wall.

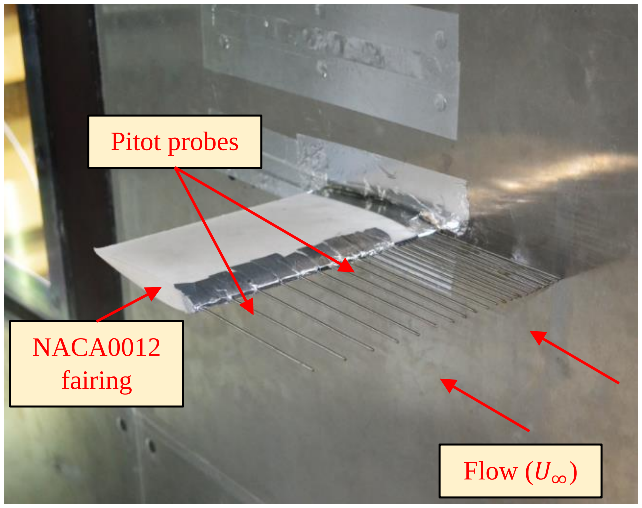


**Figure 5:** Modular boundary layer rake device installed in boundary layer wall of Stability Wind Tunnel

The corresponding time-resolved turbulence measurements were made with a high-speed stereoscopic particle image velocimetry (PIV) system. Two Phantom v2512 high-speed cameras (with Nikon 300-mm lens) were installed in the floor and were focused onto a light sheet emitted by a Photonics Industries DM series, Nd-YAG 532 $nm$ laser, with a maximum single pulse frequency of 25.6 $kHz$. The light sheet illuminates a flow seeded with atomized Propylene Glycol with an average particles size of approximately 1 $\mu m$. The cameras along with Nikon 300 $mm$ lenses were calibrated with a LaVision type $106 - 10$ two-level calibration plate using DaVis 10.0. At each measurement station, the flow-fields were sampled with different strategies to obtain fully converged statistics along with adequate spatial and temporal resolution. Two fields of view at two different sampling frequencies were taken at each condition and streamwise location. A lower sampling frequency of 1 $kHz$, provided about 24 seconds of data providing converged turbulence statistics while a superior sampling frequency of 12.8 $kHz$ for 2 seconds. The size of each data set was

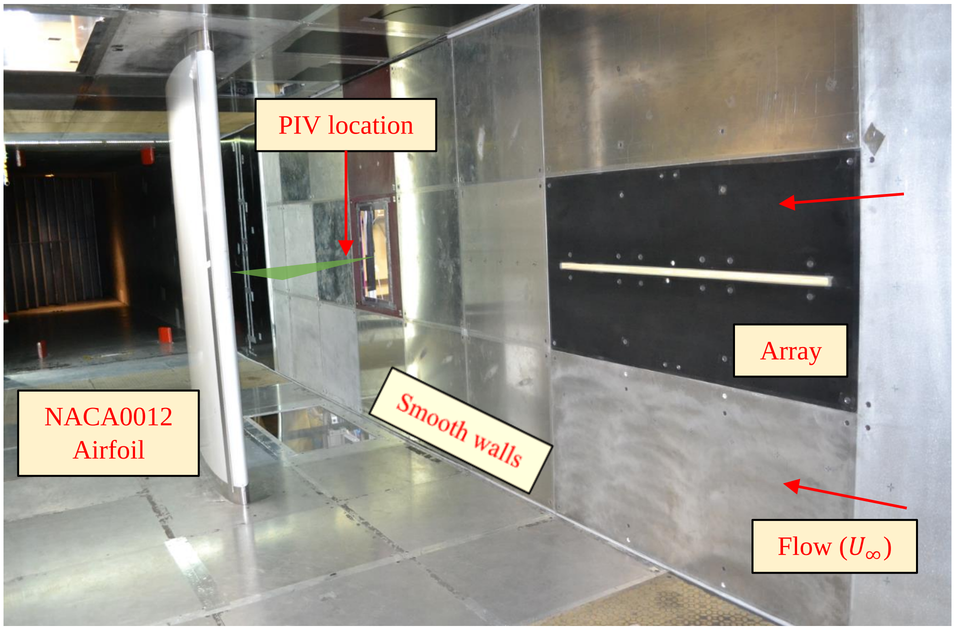


**Figure 6:** Test section of the Stability Wind Tunnel with various systems

limited by the internal storage of the camera which allows approximately 24000 images per sampling frequency. Figure 6 shows the assembled test section with various components for one measurement configuration of the pressure sensing array and the PIV.

## C. Test Matrix

Using the various instrumentation described in the previous sections, data was acquired at several streamwise distances at the mid-span of the port wall of the Stability Wind Tunnel. At these various streamwise distances, pressure gradient was controlled by sweeping the NACA 0012 from $-10°$ to $12°$ in increments of $2°$. Another variable which controlled the flow conditions was the adjustment of the freestream wind velocity. A total of 10 Reynolds numbers scaled on the airfoil chord (i.e., $0.914\ m$) were selected. The selected Reynolds numbers ranged from $7.62\ \times 10^5$ to $3.5 \times 10^6$ and were quasi-logarithmically separated from one another. For this test, the analysis is done for one of these given conditions. The data presented in the upcoming sections will include the flow conditions for 1.17 million Reynolds number, for a pressure gradient given by $0°$ angle of attack, at a location $1.164\ m$ downstream of the origin. Figure 7 shows a sample of the coefficient of mean pressure profile generated by the variation in the angle of attack of the NACA 0012 on at the midspan of the portside wall. These are generated by measuring the static pressures from pressure taps distributed along the streamwise distance of the portside walls.



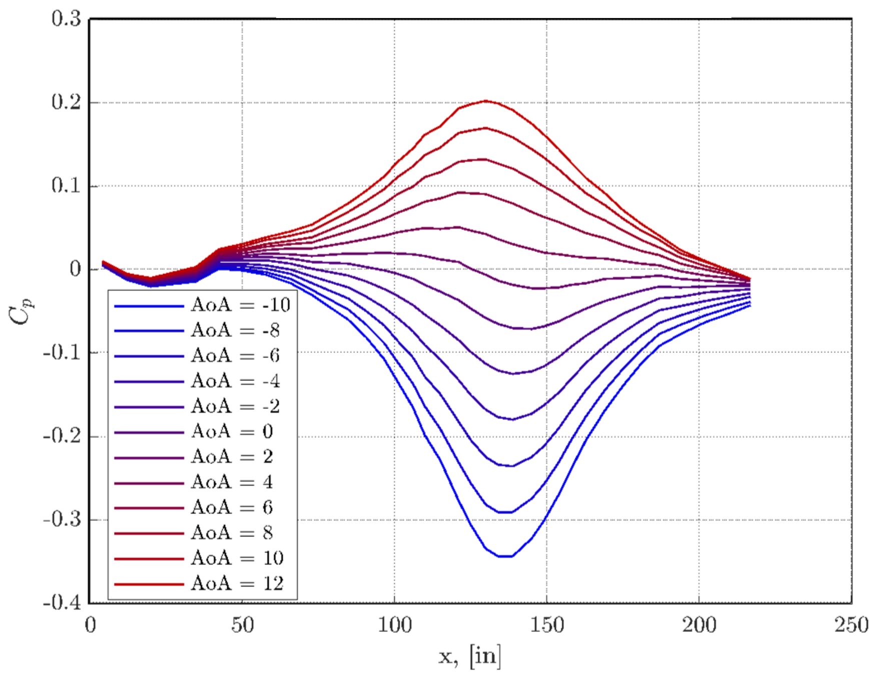


**Figure 7:** Mean pressure coefficient profile for 2 million Reynolds number case at the midspan of the port wall of the SWT

# III. Low-Wavenumber Pressure Sensing Array

The study performed by Damani [37] demonstrated the excitation of acoustic metamaterials on a non-flow side of a metasurface using turbulent boundary layer flows on the flow side. The metamaterial was in a quiescent environment while the flow was coupled with the metamaterial using a Kevlar covered half-wave cavity with a slot profile. The cavity shape had a length and width associated with it in addition to the depth, giving it a resonator characteristic. Acoustic measurements performed close to the cavity exit showed that the pressure field here was highly coherent and closely representative of the spatial average of the turbulent pressure fluctuations over the Kevlar covered cavity. In addition to this result, Damani [38] used time-resolved particle image velocimetry to show that the effects of the Kevlar covered open cavity on a turbulent boundary layer flow were negligible. This rendered the use of these resonator-based cavities as flow sensing devices which have the capabilities of wavenumber filtering.

Tests were performed on a prototype resonating sensor of the type shown in Figure 8, consisting of a Kevlar-covered quarter-wave cavity $3 \times 15$ mm in width and length, and 21 mm deep. The sensing microphone was placed at the bottom of the cavity and the sensor was tested by exposing the Kevlar covered top surface of the cavity to calibration signals as well as turbulent boundary layer pressure fluctuations. Measurements on this prototype sensor confirmed the very high coherence of pressure fluctuations at the bottom of the cavity with the top of the sensor exposed to flow and showed behavior consistent with this pressure signal representing an unweighted area average of the turbulent pressure fluctuations here.

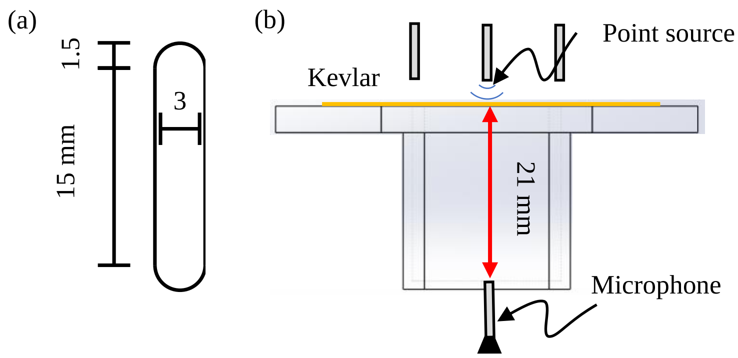


**Figure 8:** (a) Cavity profile (all dimensions in mm), (b) Schematic of tests performed on a quarter-wave cavity

## A. Array Design

The pressure sensing array comprised of 38 rectangular-shaped quarter-wave resonator cavities covered by 0.08 $mm$ Kevlar scrim (inspired from acoustic metamaterials [37]), arranged in a running bond pattern along the streamwise ($x$) direction. The array was printed in three parts using ABS Plus material on a Connex 3 printer with a layer thickness of 16 microns, which were later assembled as one unit. The array spanned a total of 1050 $mm$ in the streamwise direction with the sensors occupying a length of 961 $mm$ from the center of the first sensor to the center of the last sensor (shown in Figure 9 (a)). The profile of the resonator cavity is displayed in Figure 9 (b) along with some geometrical features to mount the array on a flat metal plate, $4' \times 2'$ in cross-section. The figure also describes the coordinate system for the resonator cavities which is consistent with the tunnel coordinates. The cavities were 50 $mm$ long in the stream direction ($x$), 3 $mm$ in the span direction ($z$) and 30 $mm$ deep ($-y$). The cavities were separated into 2 rows along the span direction by 5 $mm$ measured center to center. The streamwise separation between the

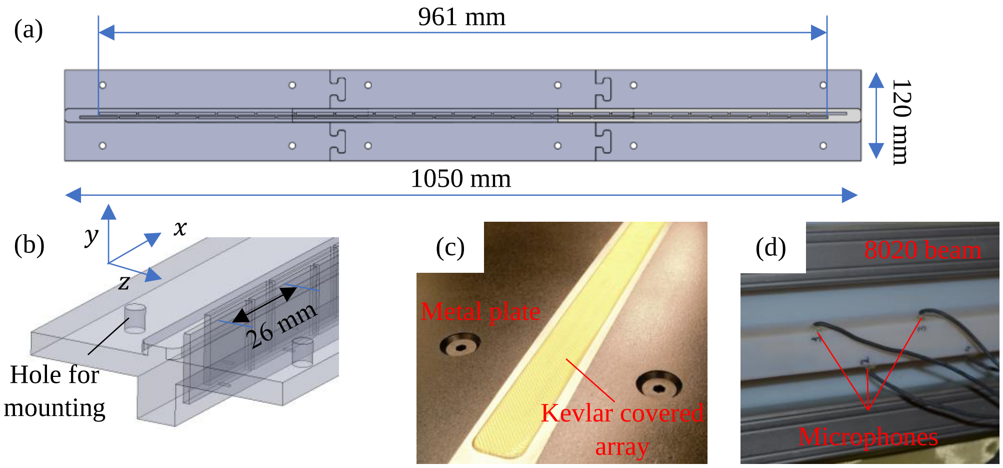


**Figure 9:** (a) Top view of pressuring sensing array, (b) Isometric view of the resonating cavities and microphone locations, (c) Top side view of assembled array with Kevlar mounted on a flat metal plate, (d) Bottom side view of the array with microphones.

cavities was $26\,mm$ which decided the wavenumber range of the system. The staggering of the adjacent rows effectively overlaps the sensors greatly reducing the streamwise aliasing of pressure fluctuations, so that simultaneous measurements with the sensors of the array can be used to determine the streamwise wavenumber transform of the wall pressure, averaged over spanwise wavenumber. The array was mounted on a metal plate such that the Kevlar covered portion was exposed on the side and was flush with the surrounding metal surface as shown in Figure 9 (c). The assembled array along with the plate was mounted at the mid height of the port wall in the test section of the tunnel. The assembled array occupied 2 panels of the test section and its position was changed along the stream direction to cover 3 sets of locations from the beginning of the test section. The array used electret condenser type, Knowles FG-23329-P07 microphones due to their flat frequency characteristics, dynamic range, and small size. These microphones were attached on the sides of the array at the bottom of the cavity sensors owing to the uniform behavior inside the cavity [37].

The resonating sensors could have a variety of shapes theoretically, but here it was decided to have a simple profile which could be rapid prototyped with precision as well as could be numerically modeled. The idea of modeling was to estimate the wall pressure fluctuations based on current models and is discussed in Section III – D. It is important to highlight here that the design of an individual sensor was based on two considerations including the flow conditions particularly the boundary layer thickness and the resonant modes associated with the cavity dimensions. The flow in the Virginia Tech Stability Wind Tunnel is typically characterized by a boundary layer thickness of about $50\,mm$ near the start of the test section where the array was installed. The length of the cavities was chosen to be $50\,mm$ such that these sensors could average over scales equivalent to the boundary layer thickness which comprised mainly of convective structures. This implied an averaging over the convective regime of the wall pressure fluctuations which made the detection of low-wavenumber pressure fluctuations possible. From the measurements performed by Damani [37], it was shown that the coherence property was limited to the modes along the length of the cavity, and this limited the frequency response of the sensors. Here, a length of $50\,mm$ corresponded to a fundamental mode of $3.4\,kHz$ which limited the response of the sensors and hence the array. The output of interest was the zero spanwise separated streamwise wavenumber frequency spectrum which implied having zero width sensors, theoretically. This was not possible practically, so a finite width of $3\,mm$ was chosen which was limited by the cleaning requirements of the rapid prototyping technology. The depth of the cavities was decided such that the fundamental mode of the sensor would lie within the first spanwise mode giving the sensor a characteristic of a second order spring-mass-damper system. Hence, a depth of $30\,mm$ was chosen for the sensor which had a resonant mode at 2.83 kHz. A schematic of the sensor is shown in Figure 10 indicating the location of the microphone.

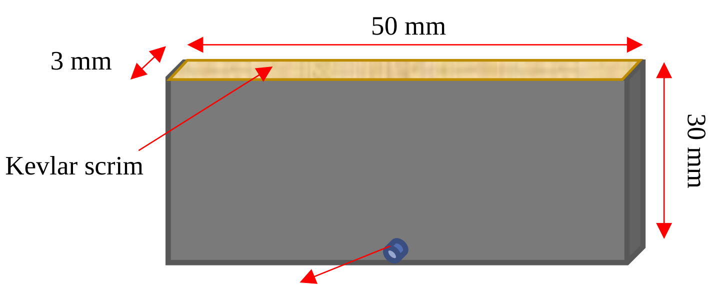


**Figure 10:** Kevlar covered resonating sensor

The shape of the sensor was chosen as a rectangle whose profile was easy to model in the wavenumber domain. Assuming a uniform sensitivity of the sensor the sensor response could be modeled as a 2D rectangular window function whose wavenumber equivalent is a 2D sinc $(\sin(x)\,/x)$ function. In order to have sufficient wavenumber resolution, the length of the array must be long. Keeping this in mind, the length of the array was chosen based on the structure of the experimental facility. The skeleton of facility was such that it could be covered with $2' \times 2'$ panels and hence the length of the array was limited to two $2' \times 2'$ panels along the flow direction, i.e., equal to the length of one $4' \times 2'$ panel. As mentioned above, aliasing is inevitable and to keep it at the minimum, the sensor spacing needs to be at least half the sensor length implying spatial overlapping of the sensors, which was not practical. To overcome this, the sensors were arranged in two rows such that the separation distance in the spanwise $(z)$ direction would be minimum i.e., the second row was as close to the first as possible, targeting the zero spanwise separation component. The second row of sensors was displaced in the streamwise direction to achieve the anti-aliasing criterion. The separation of the sensors in the streamwise ($x$) and spanwise ($z$) direction was based on the structural characteristics of the rapid prototyping technology which displayed warping for thin-walled structures. The walls had to be rigid enough to prevent structure-acoustic interaction and contaminate the response of the sensor, and to mitigate the warping of thin walls during rapid prototyping process. Based on this design, the array operating frequencies were from the lowest frequency the sensors could be calibrated (about $80\ Hz$) till the spanwise mode (about $3.4\ kHz$) and the maximum wavenumber resolved was based on the sensor separation of $26\ mm$ which corresponded to about $120\ rad/m$. The wavenumber resolution was based on the number of sensors on the array or the largest separation between sensors.

## B. Calibration

To analyze the data from the array, a calibration was performed in a large anechoic chamber with a cut-off frequency of $100\ Hz$. The setup for the same has been shown in Figure 11. It comprised of an omnidirectional speaker placed around $3.5\ m$ away from the array to be calibrated and two B&K Type 4190 reference microphones were mounted very close to the array, aligned with the middle sensor in either row of sensors. The array was mounted on a large piece of MDF board to minimize scattering effects to lower frequencies associated with the dimensions of the assembly. All sensors were calibrated in the frequency range of 80 to $6000\ Hz$. The lower limit was constrained by the anechoic chamber cut-off frequency and the higher limit was set by the speaker response.

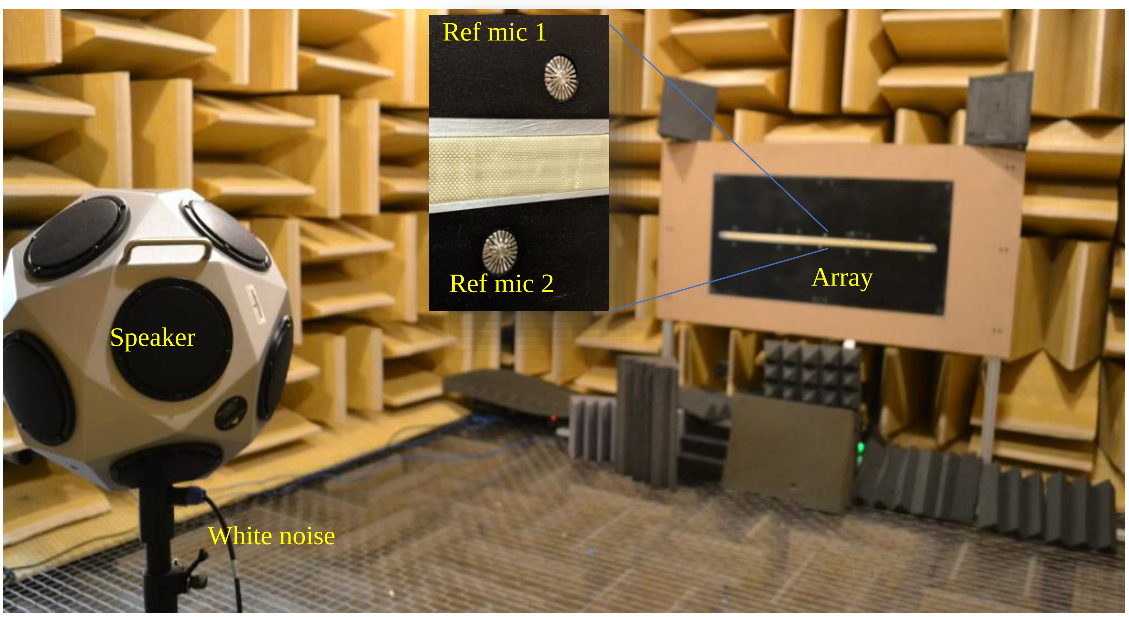


**Figure 11:** Calibration setup for pressure sensing array in a facility at Virginia Tech

The response of the individual cavity-sensors of the array is determined by finding the relation between the measured output signal of each sensor and the incident pressure on the $i^{th}$ Kevlar-covered cavity sensor. A schematic of signal flow for the calibration setup is shown in Figure 12. Here, the cavity response function to be determined is $A(\omega)$ which is given by:

$$A_i(\omega) = \frac{E[V_m^i(\omega)V_w^*(\omega)]}{E[V_p^i(\omega)V_w^*(\omega)]} \tag{1}$$

where $V_m^i$ is the signal from the cavity-sensor, $V_w$ is the signal from the white noise signal and $V_p^i$ is the signal on the Kevlar membrane of the cavity. The last of these signals ($V_p^i$) is not known but is found using the reference microphone output ($V_r$). As the reference microphone is aligned with the sensor in the center, there is a need of a time delay which corrects for the spatial difference between the reference microphone and any $i^{th}$ sensor. Hence, the signal at the surface of any $i^{th}$ sensor would be

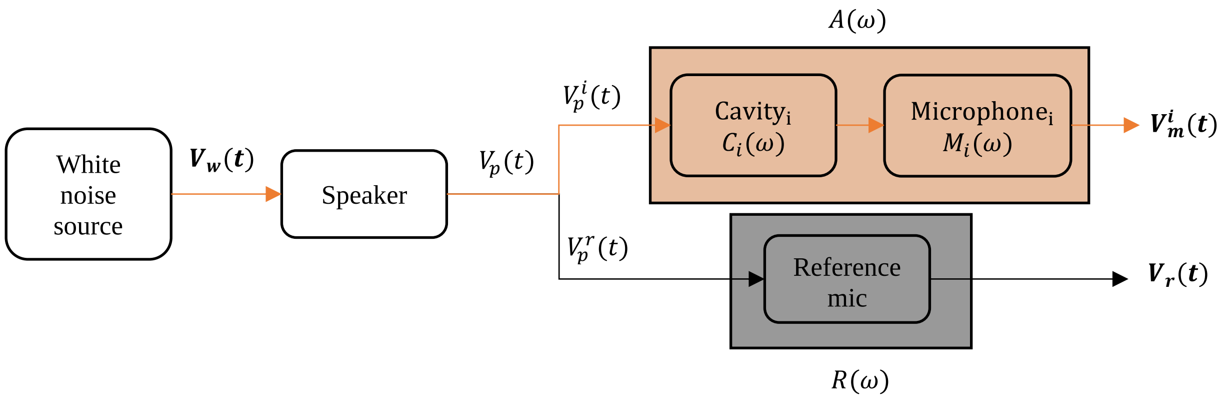


**Figure 12:** Schematic of signal flow for the calibration setup

$$V_p^i(\omega) = V_r(\omega)/R(\omega)e^{j\omega\tau_i} \tag{2}$$

where $\tau_i$ is the time-delay between the reference microphone and $R(\omega)$ is the reference microphone response function. The time delay for the $i^{th}$ cavity was found by fitting a linear curve to the response function of the $i^{th}$ cavity without any time delay. This reduces the cavity response function to:

$$A_i(\omega) = \frac{E[V_m^i(\omega)V_w^*(\omega)]}{E[V_r(\omega)/R(\omega)e^{j\omega\tau_i}V_w^*(\omega)]} = \frac{G_{mw}^i(\omega)}{G_{rw}(\omega)}R(\omega)e^{-j\omega\tau_i} \tag{3}$$

where $G_{mw}^i(\omega)$ is the cross-spectrum between $i^{th}$ sensor and the white noise source and $G_{rw}(\omega)$ is the cross-spectrum between reference microphone and the white noise source. The calibration of the array yields response functions which show effects of scattering from the edges in frequency range of 200 to 800 $Hz$. These effects were prominent for sensors away from the reference microphone i.e., closer to the edges of the MDF. This suggests that this calibration scheme was not ideal as it involved sources of errors and work is being done to improve on this technique for future arrays. The response function from calibration (Eq. (3)) was fitted with a smoother curve to minimize the uncertainties

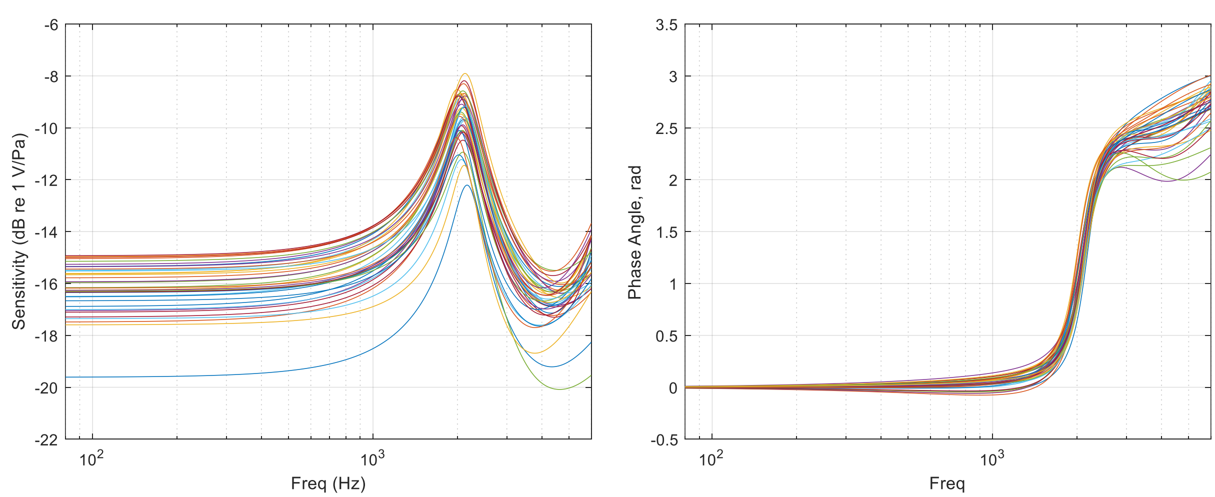


**Figure 13:** *Left:* Amplitude calibrations; *Right:* Phase calibrations for all 38 sensors on the array

in phase and to avoid the scattering effects affecting the data processing. These fitted amplitude and phase corrections are shown in Figure 13. The amplitude corrections show a second order system behavior with a peak corresponding to the fundamental resonant mode of the cavity (about $2200\ Hz$). A $30\ mm$ deep cavity exhibits a resonant mode of $2833\ Hz$ theoretically, but this is reduced in practicality due to end effects and the presence of Kevlar which broadens the peak. The rise in the response function beyond the first peak occurs as the fundamental mode along the length of the cavity is approached. However, this is not of importance as the calibrations are valid only till about $6000\ Hz$.

## C. Data Acquisition and Processing

The microphones used for the sensors were connected to Type 3050 LAN-XI DAQ modules using BNC cables. An intermediate connection to DB25 Breakout Board was used to supply the microphones with a DC supply of $1.5\ V$ and for grounding. Data was recorded with a sampling frequency of $65536\ Hz$ for 32 seconds. The processing of data from the array involved the tunnel flow conditions such as the velocity and Mach number which were obtained from the mean pressure data from the tunnel as temperature in the contraction and the static pressure in the settling chamber.

As mentioned earlier, one way to study the wall pressure fluctuations is to look at the wavenumber – frequency spectrum. The wavenumber – frequency spectrum of the wall pressure is defined as the Fourier transform of the space-time correlation function which is given by

$$R(\zeta,\eta,\tau) = \overline{p(x,z,t)p(x+\zeta,z+\eta,t+\tau)} \tag{4}$$

Here, $(\zeta,\eta)$ is the separation between two points in the $x-z$ plane of the array as defined in Figure 9, and the $\bar{p}$ indicates an expected value. The spectrum requires the Fourier transform in space and time; hence the process is split into two: transforming in time first to obtain the cross-spectral density and then transforming in space to obtain the wavenumber – frequency spectrum. The cross-spectral density is obtained as

$$G(\zeta,\eta,\omega) = \frac{1}{2\pi}\int_{-\infty}^{\infty} R(\zeta,\eta,\tau)\, e^{i\omega\tau} d\tau. \tag{5}$$

The wavenumber transform becomes as follows

$$\Phi(k_x,k_z,\omega) = \frac{1}{(2\pi)^2}\int_{-\infty}^{\infty}\int_{-\infty}^{\infty} G(\zeta,\eta,\omega)\, e^{-i(k_x\zeta+k_z\eta)} d\zeta d\eta. \tag{6}$$

Inverse transforming in $k_z$ then gives the streamwise wavenumber frequency transform as a function of separation $(\eta)$

$$\phi(k_x,\eta,\omega) = \int_{-\infty}^{\infty} \Phi(k_x,k_z,\omega) e^{ik_z\eta} dk_z \tag{7}$$

These definitions assume that the pressure fluctuations are stationary in time and homogeneous in the $x-z$ plane. This assumption is good for time stationarity and homogeneity in the $z$ direction, but the homogeneity in the stream $(x)$ direction is limited. As the data is sampled for a finite time period and the array spans a finite region with its sensor distribution, the above relations reduce to discrete transforms when applied to the measurements. The cross-spectral density, Eq. (5) is calculated as

$$G_{ab}(\zeta,\eta,\omega)^{(m)} = \frac{\Delta t}{2\pi N N_{rec}\overline{w^2}} \sum_{p=1}^{N_{rec}} DFT^*\big(b_n^{(p)} w_n\big) DFT\big(a_n^{(p)} w_n\big) \tag{8}$$

where $\Delta t$ is the sampled time frame, $N_{rec}$ are the number of records the signal is divided into, $N$ is the number of samples inside one record, $\overline{w^2}$ is a factor for the window type used, $DFT$ represents the numerical Fourier transform operation and $a_n w_n, b_n w_n$ denote the sensor output signal multiplies with a window function. The summation is done over all records implying ensemble averaging. In a similar manner the auto-spectrum of a sensor could be obtained by setting the input as the same sensor signal instead of a different sensor. A single sided auto-spectrum was evaluated for all the sensors on the array. The spectrum evaluation used a record length of 8192 samples with 50% overlap. Each record was windowed using a Hanning window ($\overline{w^2} = 3/8$) and the sampling frequency and record length gave a frequency resolution of 8 $Hz$.

The calibration for each sensor was then applied to the frequency spectrum which corrected for the amplitude and phase of individual sensor giving the measured signal as pressure fluctuation. The calibration corrected the auto-spectra by dividing out the magnitude of the response function of each sensor while the cross-spectra were corrected by dividing the product of respective sensors. As the array comprised of 38 sensors spaced uniformly in a streamwise direction with a small displacement in the spanwise direction to accommodate the sensors, the cross-spectral density of sensors could be assumed to be a function of only the streamwise distance. Each combination of sensors indicated some spatial separation in the $x$ direction, however some of which were repeated. For instance, the very first sensor in line and the one next to it (displaced 26 $mm$ in $x$ from the first) gave one pair. Another pair could be sensor 2 – 3, 3 – 4 and so on. This could be done for farther spaced sensors as well such as sensor 1 – 4, 2 – 5 and so on, but for each separation the number of combinational pairs reduced. Hence, the cross-spectrum for each spatial separation could be averaged over the number of combinations for that separation to obtain an averaged cross-spectral matrix. The averaged cross-spectral matrix was then numerically Fourier transformed in streamwise distance, using a Nuttall window to obtain an estimate of the streamwise wavenumber frequency spectrum of Eq. (7), for zero spanwise separation $\eta$. Theoretically, an infinitely thin sensor in the spanwise direction i.e., zero thickness in the $z-$ direction would average over all the spanwise wavenumbers giving rise to a wall pressure spectrum as a function of zero spanwise separation i.e., $\eta = 0$ in Eq. (7). Here, the sensors were displaced in the spanwise direction for anti-aliasing, and this implied that the sampled wall pressure fluctuations could be assumed to be at zero separation in the spanwise direction. This assumption simplifies the data analysis process however the results do not represent the wall pressure spectrum at zero separation rather a small finite separation of 5 $mm$.

## D. Array Modeling

A mathematical model was developed to estimate the accuracy of the array measurements and to reveal sources of error as has been done in previous studies [11][14]. This particularly involves a convolution of the wavenumber response of the array of sensors with a known wall pressure spectrum model [5][9]. The wavenumber response of the array is determined from the individual sensor response and the response due to the sensor arrangement. The uniform individual sensor response implies a sinc function (Eq. (9)) in wavenumber space with the arguments as the sensor physical dimensions with $l$ as the length of the sensor in $x$ and $w$ as the width of the sensor in the $z-$direction.

$$A^m(\boldsymbol{k}) = \frac{1}{(2\pi)^2}\frac{1}{k_x l/2}\frac{1}{k_z w/2}\sin\left(\frac{k_x l}{2}\right)\sin\left(\frac{k_z w}{2}\right) \tag{9}$$

The arrangement of the sensors was incorporated as a complex exponential with an argument of the spatial separation between the sensors. Hence, the measured cross-spectrum ($S_{qq}$) from the array of sensors could be modeled as

$$S_{qq}(\boldsymbol{\Delta y}, \omega) = \iint_{\infty} \phi_{pp}(\boldsymbol{k}, \omega)|A(\boldsymbol{k})|^2 e^{i\boldsymbol{k}.\boldsymbol{\Delta y}} dk_1 dk_3 \tag{10}$$

where $\phi_{pp}$ is the wall pressure spectrum from the Chase model [9], $A(k)$ is the wavenumber transform of the sensor spatial sensitivity and the exponential term accounts for the sampling in space by the spatially distributed sensors. Here, the array comprised of a streamwise distribution of sensors in 2 rows with every sensor in the second row shifted by 26 $mm$ in the $x-$ direction while 5 $mm$ in the $z-$ direction with respect to the sensor in the first row. Cross spectral estimates from Eq. (10) were then numerically Fourier transformed in $x$ in the same manner as the measurements to obtain estimates of the streamwise wavenumber frequency spectrum. Comparisons of these with the original Chase spectrum model then provided estimates of measurement errors.

## IV. Results and Discussion

Experiments were performed for a variety of Mach number and pressure gradient flows, with the array subjected to various boundary layer conditions. However, this paper focuses only on results with the zero-pressure gradient when the array was located at the beginning of the test section for an airfoil chord Reynolds number of 1.17 million. The boundary layer conditions for this case were measured using the BL Rake at $x = 1.164\ m$ from the start of the test section. This position corresponded to a location just upstream of the very first sensor of the array. The boundary layer properties at this location have been summarized in Table 1. These indicate the flow to be a high Reynolds number but low Mach number flow.

**Table 1:** Boundary layer properties over the array

| | |
|---|---|
| Free stream velocity ($\boldsymbol{U_\infty, m/s}$) | 22.37 |
| Edge Velocity ($\boldsymbol{U_e, m/s}$) | 22.077 |
| Boundary layer thickness ($\boldsymbol{\delta, mm}$) | 54.21 |
| Displacement thickness ($\boldsymbol{\delta^*, mm}$) | 7.834 |
| Friction velocity ($\boldsymbol{U_\tau, m/s}$) | 0.828 |
| Momentum thickness ($\boldsymbol{\theta, mm}$) | 5.91 |
| Reynolds number per meter ($\boldsymbol{Re/m}$) | 1424627.62 |
| Momentum Thickness Reynolds number ($\boldsymbol{Re_\theta}$) | 7627.7 |
| Reynolds Number ($\boldsymbol{Re_\tau}$) | 286.8 |
| Shape Factor, (**H**) | 1.33 |
| Mach number on freestream ($\boldsymbol{M_\infty}$) | 0.0657 |

The normalized boundary layer profile for this case is shown in Figure 14 (a) below. In this figure, the boundary layer thickness is selected to be the distance normal from the wall where the local streamwise velocity component becomes equal to 99% of the freestream velocity, which is termed as the edge velocity, $U_e$. The flow characteristics extracted from the boundary layer rake measurements were then used later in the acoustic analysis for the low-wavenumber pressure sensing array. Figure 14 (b) shows a plot of the boundary layer profile in wall units. This profile is plotted on a standard Spalding [36] profile for this condition. Boundary layer profiles measured downstream at $x = 2.47\ m$

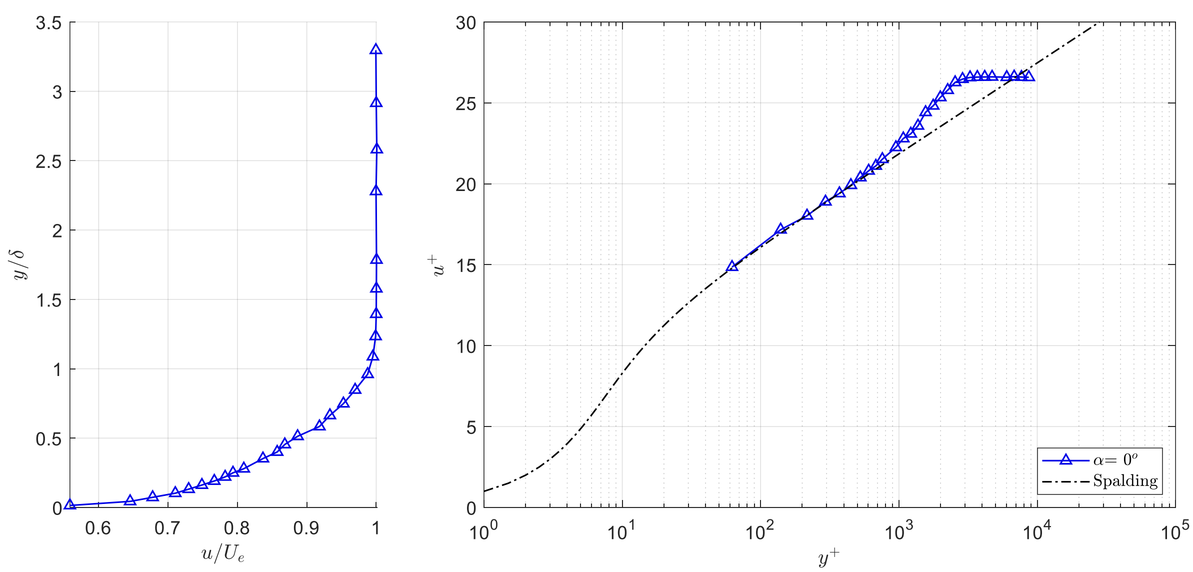


(a) (b)

**Figure 14:** (a) Normalized boundary layer profile on the boundary layer thickness; (b) Boundary layer profile at Re = 1.17 million superimposed with the Spalding profile

for this flow condition showed no significant change in the flow profile and a growth in the boundary layer thickness to $67.1\ mm$, and a change in momentum thickness Reynolds number to $Re_\theta = 9382.8$ and a shape factor of $H = 1.31$. Comparing this to the boundary layer characteristics measured upstream of the array, at $x = 1.164\ m$ from the origin, where the boundary layer thickness was $\delta = 54.2\ mm$ and the momentum thickness-based Reynolds number ($Re_\theta$) was $7627.7$ with a shape factor ($H$) of $1.33$. The thickness of the boundary layer grew by $12.9\ mm$ over a streamwise distance of $1.3\ m$.

These results were also confirmed through PIV measurements. Particle Image Velocimetry (PIV) and acoustic measurements were conducted at different locations within the test section at various pressure gradients and Reynolds numbers. This study focuses on the zero-pressure gradient case at a location upstream of the airfoil as exemplified in Figure 6. The Reynolds number based on the chord of the airfoil for this case was 1.17 million with a freestream velocity of 20.4 m/s. This was equivalent to $Re_\theta$ = 6830. The data collected using PIV was processed to obtain the boundary layer velocity profiles and the Reynolds stresses as shown in the figures. This data was then compared to the results obtained by DeGraaff and Eaton [39] which was collected for a flow over a flat plate at $Re_\theta$ = 5200. The data is normalized on the inner scaling including the friction velocity ($u_\tau$) and the kinematic viscosity ($\nu$). In Figure 15 (a), the mean velocity profile obtained follows a similar trend to the flat plate results [39], both of which can be accurately described by the log law. The Reynolds stresses obtained are also comparable to the DeGraaff and Eaton [39] results as shown in Figure 15 (b) and this indicates good PIV data. The non-dimensional Reynolds stress obtained from the PIV is seen to fall off below about $y^+ = 200$, a result that is due to under-resolution of the $v -$ component

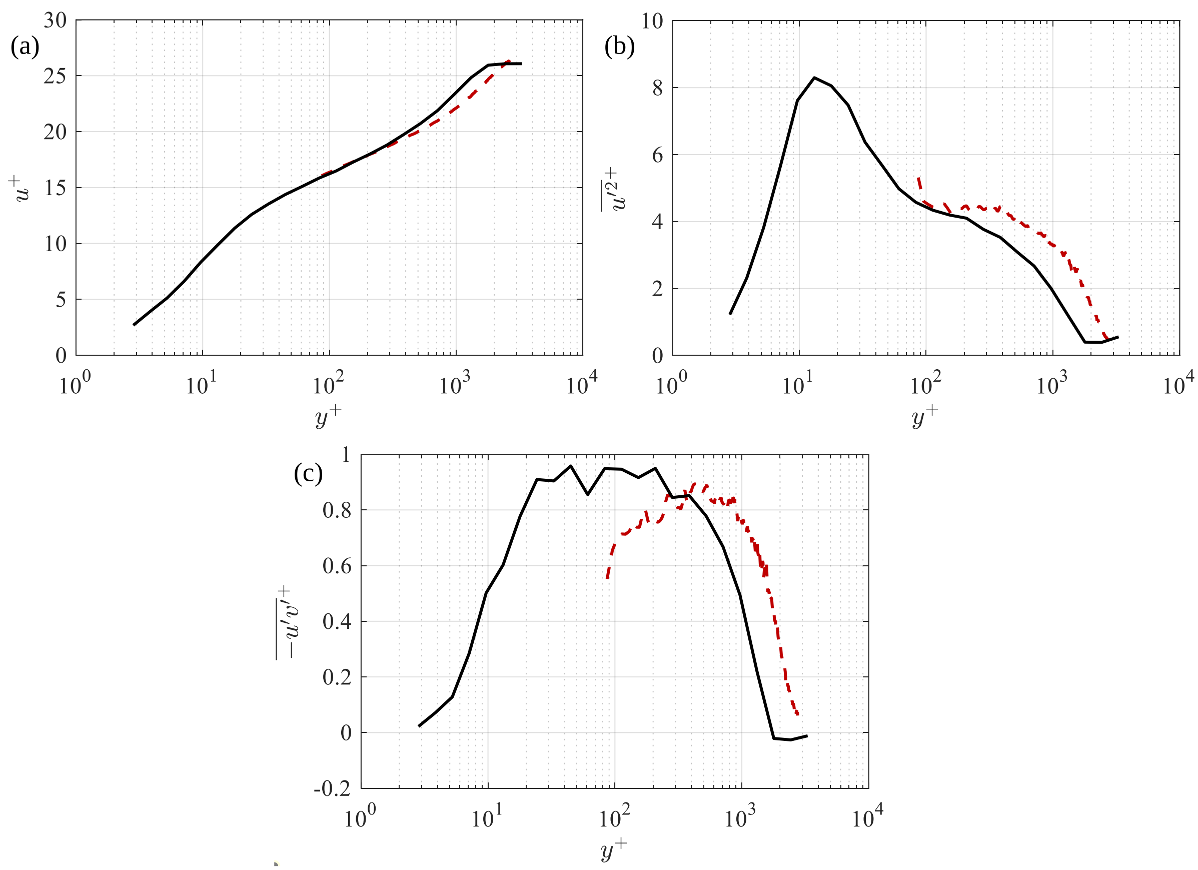


**Figure 15**: (a) $u^+$, (b) $\overline{u'^2}^+$, (c) $\overline{-u'v'}^+$ profiles vs normalized wall normal distance ($y^+$) for a flow with zero pressure gradient ($Re_\theta = 6830$, dashed). All plots compared to DeGraff and Eaton flat plate data for a zero-pressure gradient flow at $Re_\theta = 5200$ (solid).

fluctuations near the wall.

In the array, 38 measurement sensors were located every $26\ mm$ from $x = 1.614$ to 2.833. Figure 16 (a) shows the surface pressure auto-spectra from all sensors in decibels (dB re 20 $\mu Pa$) after applying the calibrations of each sensor, as a contour map. The abscissa represents the streamwise separation distance $x - x_o$ from the location of the most upstream sensor. The ordinate plots the frequency on a logarithmic axis in $Hz$ and is limited by the spanwise mode of the sensor. On the color scale, red represents high levels while the blue represents low levels in $dB$. One can see a general decreasing trend with frequency which is a characteristic of the wall pressure fluctuation over a smooth wall. The spectrum appears streamwise homogeneous with a sensor-to-sensor uncertainty of about $\pm 1.5\ dB$ at all frequencies. Line plots of the auto-spectra as a function of frequency normalized on inner scales are shown in Figure 16 (b). The dark blue lines refer to the positions upstream, green corresponds to sensors in the center of the array and the bright red to the most downstream section of the array. The black dashed line shows the normalized point pressure auto-spectrum measured at $x = 1.21\ m$ in this flow but at a higher flow speed of $35\ ms^{-1}$ [32]. The solid line shows the point-pressure auto-spectrum implied by the Chase model for the boundary layer scales. The red dashed line shows the same Chase spectrum but calculated by accounting through the spatial averaging of each array sensor, according to Eq. (10). The array sensor spectra fall well below the pointwise pressure spectra and the difference increases with increasing frequency. This, of course, is due to the attenuation of small-scale pressure fluctuations by area averaging. The array sensor spectra appear quite closely consistent with estimates made using Eq. (10), particularly in the mid frequency range. There appears to be a discrepancy in the levels between Chase and the measured array which could be due to a scaling factor but the averaging by the array seems evident.

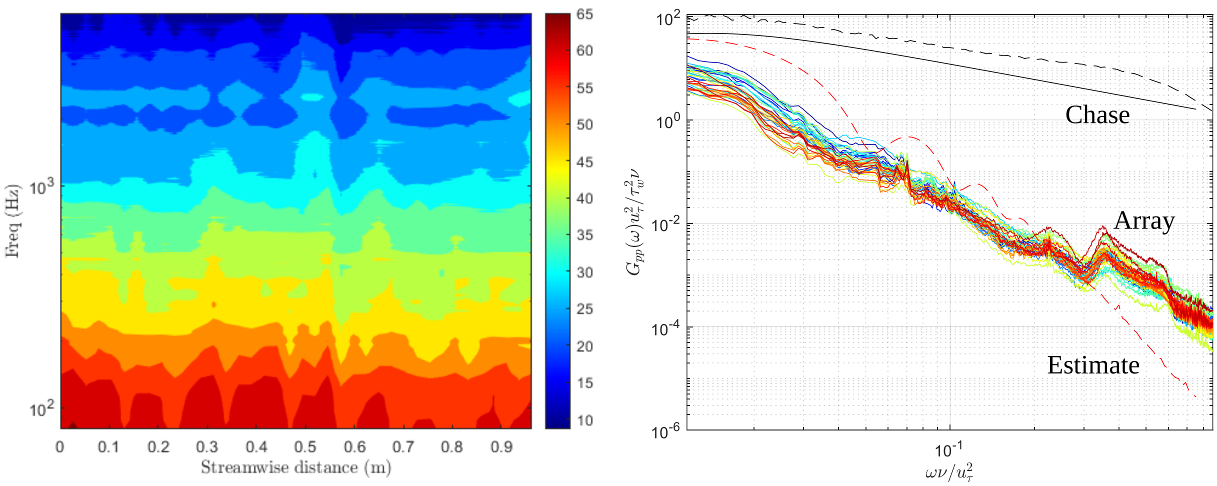


(a) (b)

**Figure 16:** (a) Contour map of the auto-spectrum in $dB$ as a function of frequency and distance; (b) Line plots of normalized Autospectrum as a function of normalized frequency on inner scales ($u_\tau, \tau_w$)

The magnitude of the averaged cross-spectrum matrix (in decibels) obtained with the array is shown in Figure 17, as a function of frequency and streamwise separation ($\Delta x$). For $\Delta x = 0$ this plot represents the average auto-spectrum of all 38 sensors. The contour map shows a drop in cross-spectral density levels with frequency. One can also see subtle patterns/fringes which we suspect are manifestations of imperfections in the wavenumber response of the array. At certain frequencies, there are horizontal bands which indicate acoustic noise or sound as these span all sensors. There are features running diagonally across the contour with weaker magnitude and these indicate the sub-convective structures but this not very apparent till the wavenumber transform is taken. The frequency – spatial separation decomposition is transformed into a streamwise wavenumber – frequency spectrum by Fourier transforming along the separation. During this process the cross-spectral matrix is conjugate flipped and windowed to obtain less spectral leakage to higher wavenumbers.

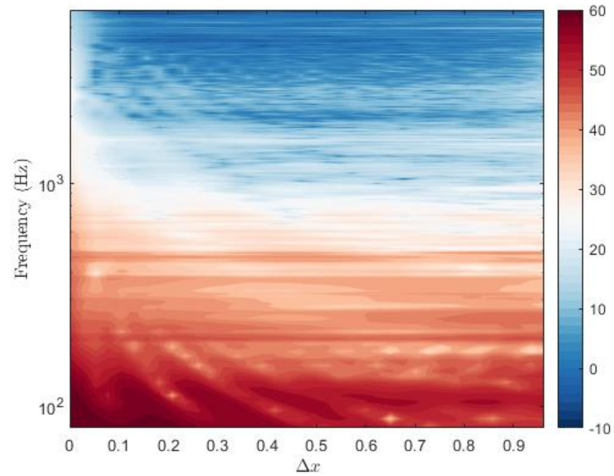


**Figure 17:** Contour plot showing the averaged cross-spectral matrix as a function of frequency and streamwise separation.

The wavenumber – frequency plot is shown in Figure 18 (a) with the streamwise wavenumber ($k_x$) on the $x$ −axis and the frequency on the $y$ −axis on a logarithmic axis. A black dashed line represents the convective ridge line based on the boundary layer parameters and the red dashed line represents the sound line. The color scale represents the magnitude of the Fourier transformed cross-spectral matrix (Figure 17) in $dB$. The frequency limits have been cut-off at $3450$ $Hz$ which corresponds to the resonant mode of the cavity along its length. There is a large dynamic separation between the acoustic and convective regime which is referred to as the sub-convective regime. The array can separate the acoustic and convective features as seen from the two distinct red contours. For the low-speed flow studied here, the area between the convective line and the sound line is large with the convective ridge limited to low frequencies (about 300 Hz). Acoustic features are visible at low frequencies and wavenumbers along the sound line. Further along the sound line these features become feeble although traces of it can be seen especially at higher frequencies. A feature at about 500 Hz lying between the two lines is suspected to be due to the folding back of the convective ridge owing to the sensor wavenumber response side lobes.

Figure 18 (b) shows the wavenumber – frequency spectrum as a function of normalized frequency and wavenumbers. The spectrum is also normalized on the boundary layer parameters such as the displacement thickness, wall shear

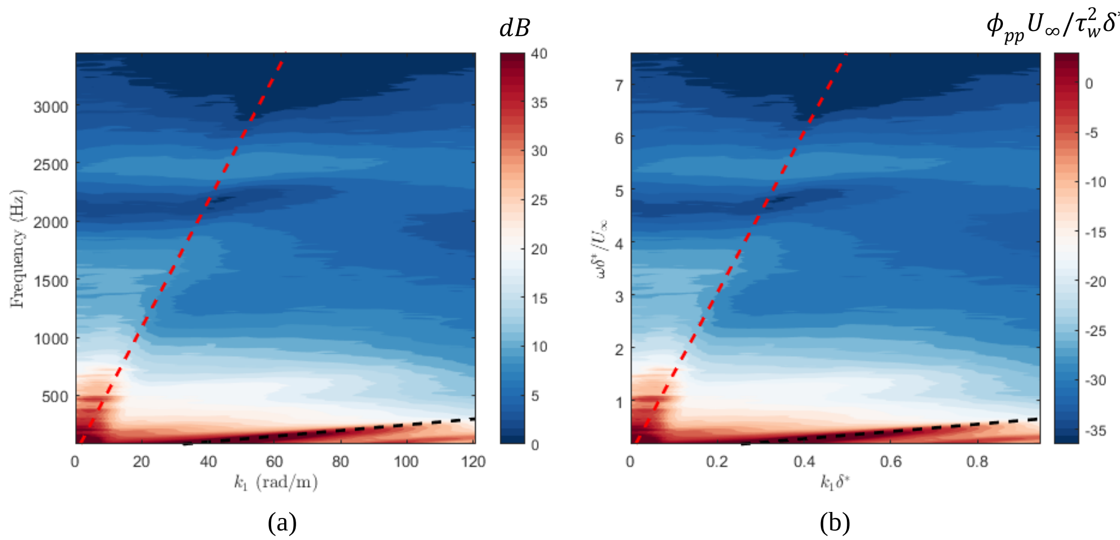


**Figure 18:** Wavenumber – frequency contour plot for a flow at $M_\infty = 0.066$ in zero pressure gradient (a) in SPL levels; (b) Normalized on boundary layer parameters ($\delta^*, \tau_w, U_\infty$)

stress and the flow speed. A general decreasing trend with increasing frequency is seen with the exception that the levels increase over the convective ridge and the acoustic cone. Some features in the sub-convective regime such as the one at about 2500 Hz corresponds to the resonant mode of the sensor. These features are better visualized when constant wavenumbers are picked on this plot and the variation is seen as a function of frequency.

The wavenumber – frequency plot can be compared to the comprehensive Chase model [9], also discussed by Blake [1] in detail. The model represents a three-dimensional plot with the wavenumbers in streamwise and spanwise direction of flow as well as frequency. However, here the array measures data at zero spanwise wavenumber which represents a planar section corresponding to zero spanwise wavenumber of the Chase model. The Chase model was modeled with sufficient range and resolution to capture the spectrum for which a convergence study was performed with varying range and resolution and study the effects on the predictions. A grid resolution with 400, 1210 and 820 points were chosen along the frequency, streamwise ($k_x$) and spanwise ($k_z$) wavenumber, respectively. Figure 19 shows the zero-spanwise-separation wavenumber – frequency wall pressure spectrum as predicted by Chase (black) and the one obtained from the array (red) at three streamwise wavenumbers corresponding to $k_1\delta^* = 0.148, 0.398$ and $0.625$ as a function of frequency. The y – axis shows the levels of the spectrum in $dB$ rel 20 $\mu Pa$ and the x – axis shows the frequency. There is a clear difference in levels seen between the two plots and is suspected to be due to a scaling factor but overall, the sub-convective features are seen to be captured by the array. The array data does not extend to lower frequencies due to limited frequency band of calibration and the microphone response. There are some bumps seen in the array data which are due to the convective ridge folding back into low wavenumbers which was also seen in Figure 18. The peaks at higher frequencies are due to the resonant mode of the sensor. This clearly shows that the array can measure wall pressure spectrum using resonating cavities and the levels measured are comparable to those implied by the Chase spectrum.

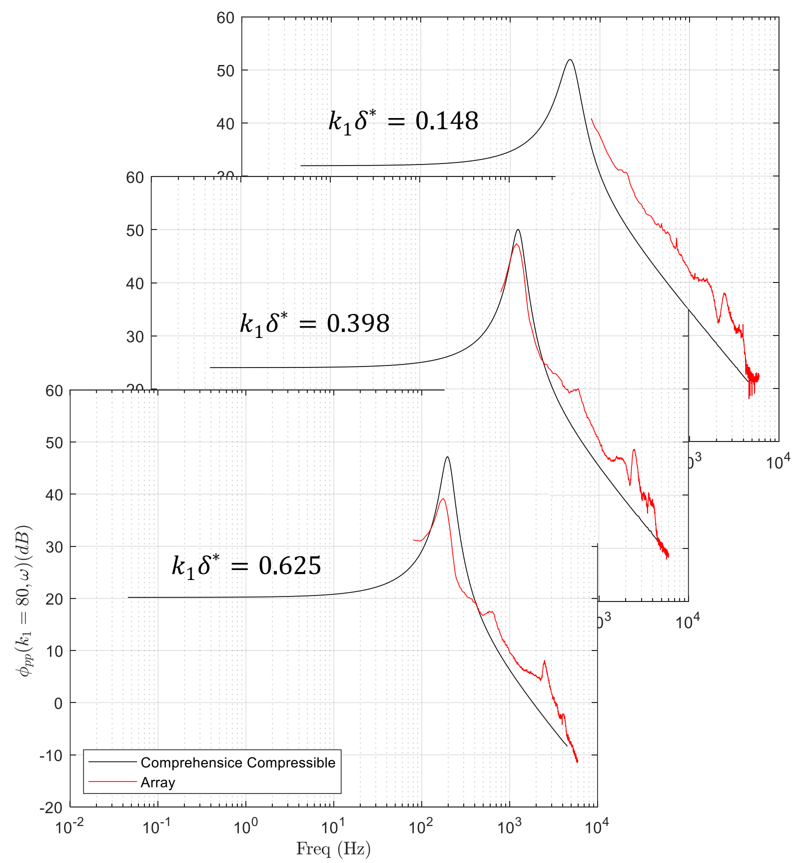


**Figure 19:** Measured wavenumber – frequency plot at zero spanwise wavenumber and a streamwise wavenumber of 19, 51 and 80 $rad/m$ from the top to the bottom compared with Comprehensive Chase model [9].

Results from modeling the array response at the boundary layer conditions are shown in Figure 20. The wavenumber – frequency spectrum using Chase model is shown in Figure 20 (a) and it was obtained by integrating over the spanwise wavenumbers of the 3D spectrum shown in Figure 1. The x – axis represents the streamwise wavenumber ($rad/m$) while the y – axis is the frequency in $Hz$. The Chase model predicts the convective ridge, and this is seen as contours of constant levels around the convective line. The Chase does not capture the acoustics as these features are not modeled in the definition. Estimates of the wavenumber – frequency spectrum found using Eq. (10) is shown in Figure 20 (b). The estimate uses the Chase model for the wall pressure spectrum but convolves it with the array response. This introduces features in the spectrum some of which correspond to the averaging behavior of the sensor while others due to the sensor wavenumber response. In Figure 20 (b), the convective ridge seems to be cut short compared to the Chase model which is due to the averaging behavior of the sensor. A feature at about 500 Hz is an artifact seen due to the finite spanwise separation of sensors. A model with zero spanwise separated sensors (a hypothetical case) yields an estimated spectrum with no such feature. There is a secondary lobe seen in the modeling which occurs due to the folding of the aliased convective ridge from wavenumber response of the sensor. The acoustic line is not captured by the modeling as the Chase model does not contain acoustics. Above a frequency of about 1000 Hz, there are ridges observed which are an artifact of the wavenumber response of the sensor. This suggests that the modeling can estimate the averaging by the sensor, however, it requires further investigation on the mathematical model of the sensor as it seems to introduce aliasing.

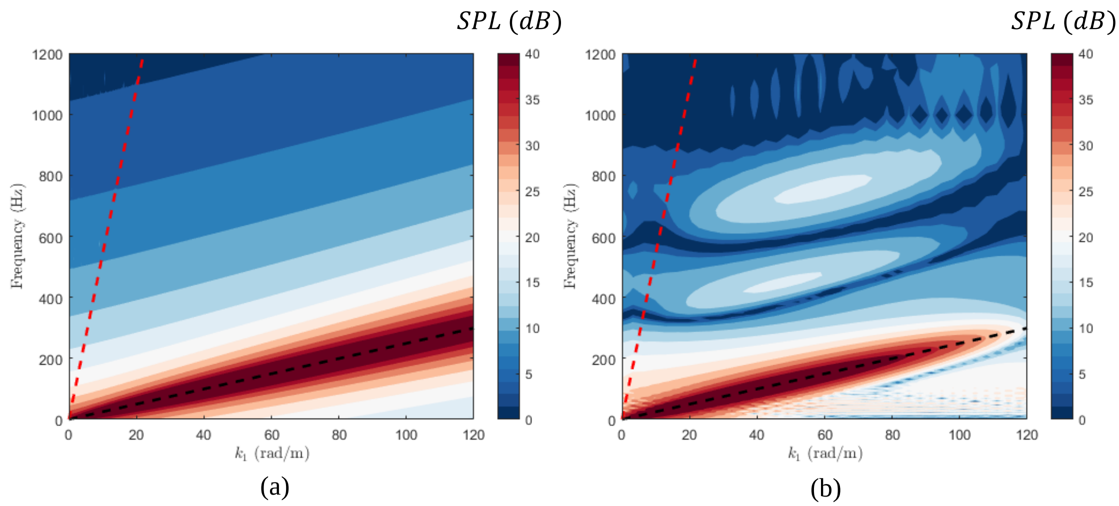


**Figure 20:** (a) Modeled Chase Spectrum (b) Modeled Array Spectrum. Acoustic line (red), Convective line (black)

## V. Conclusions

An extensive set of measurements was acquired in a wind tunnel to study the low-wavenumber characteristics of the wall pressure fluctuations in the presence of adverse, favorable and zero pressure gradients using an array of Kevlar covered resonating sensors. The study presented here focuses on a single flow case with zero-pressure gradient. The boundary layer parameters were documented using Pitot rake and particle image velocimetry measurements. This paper describes the design of a possible array of sensors inspired by acoustic metamaterials along with its calibration process. The calibration reveals scattering effects using regular calibration schemes, and refined procedures need to be investigated to calibrate such arrays. Analytical modeling of the array response with existing wall pressure models is introduced, and its results are compared with the experimental results. The modeling shows fair agreement with the data although some discrepancies are seen due to assumptions of the sensor spatial sensitivity during modeling. The results show that the array is successful in filtering out wavenumbers larger than the one associated with the sensor length scale which dampens the convective regime of the wall pressure fluctuations and gives better signal-to-noise ratio in the sub-convective regime. Some features in the sub-convective region especially at low frequencies and wavenumbers suggest aliasing due to the sensor shape. It is surprising to see faint features along the acoustics line at higher frequencies suggesting filtering of acoustics as well. The measured data from the array of sensors at low Mach number and high Reynolds number was compared with the comprehensive Chase model [9] evaluated at the same flow conditions as the measurements. The comparison revealed a difference in levels between the model and the measurements which was seen to be increasing with wavenumber. The measurements revealed artifacts due to the aliasing from the array; however, the convective peak was captured relatively nicely. This study showcases the feasibility of an array of resonating sensors to measure low-wavenumber pressure fluctuations beneath a turbulent boundary layer. It highlights the importance of the effects of the sensor shape and their distribution on the measured spectrum and suggests designing optimized arrays with lower aliasing and higher resolution.

In future work, the relation of the low-wavenumber pressure fluctuations with pressure gradients and flow speeds would be explored from the data collected in this experiment, and optimized arrays would be developed based on numerical modeling of the array with different configurations and shapes.

**Acknowledgments**

The authors would like to thank the Office of Naval Research, in particular Dr. Ki-Han Kim for his support under grant N00014-20-1-2821. The authors would also like to thank ONR and Dr. Greggory Orris for their support of aspects of the sensor development, under grants N00014-21-1-2500 and N00014-18-1-2179. We are extremely grateful for the contributions of Bill Oetjens, Ben Judelson, Vidya Vishwanathan, Daniel Fristch, and Aldo Garguilo to wind tunnel testing. We also thank the Virginia Tech Aerospace and Ocean Engineering Machine Shop headed by Mr. James Lambert for their support in designing and manufacturing test hardware and instrumentation.

## References

[1] Blake, W.K., *Mechanics of Flow-Induced Sound and Vibration, Volume 2: Complex Flow-Structure Interactions*. 2017: Elsevier Science.

[2] Graham, W.R., *A Comparison of Models for the Wavenumber-Frequency Spectrum of Turbulent Boundary Layer Pressures.* Journal of Sound and Vibration, 1997. 206(4): p. 541-565.

[3] Liu, Y. and A.P. Dowling, *Assessment of the Contribution of Surface Roughness to Airframe Noise.* AIAA Journal, 2007. 45(4): p. 855-869.

[4] Juvé, D., et al., *Measurements of wall pressure wavenumber- frequency spectra: experimental challenges and some recent advances*, in *Flinovia 3*. 2019: Lyon, France.

[5] Corcos, G.M., *The Resolution of Turbulent Pressures at the Wall of a Boundary Layer.* Journal of Sound and Vibration, 1967. 6(1): p. 59-70.

[6] Bull, M.K., *Wall-pressure fluctuations associated with subsonic turbulent boundary layer flow.* Journal of Fluid Mechanics, 1967. 28(4): p. 719-754.

[7] Willmarth, W.W., *Pressure Fluctuations Beneath Turbulent Boundary Layers.* Annual Review of Fluid Mechanics, 1975. **7**: p. 13-38.

[8] Chase, D.M., *Modeling the Wavevector-Frequency Spectrum of Turbulent Boundary Layer Wall Pressure.* Journal of Sound and Vibration, 1980. 70(1): p. 29-67.

[9] Chase, D.M., *The Character of the Turbulent Wall Pressure Spectrum at Subconvective Wavenumbers and a Suggested Comprehensive Model.* Journal of Sound and Vibration, 1987. 112(1): p. 125-147.

[10] Maidanik, G. and D.W. Jorgensen, *Boundary Wave-Vector Filters for the Study of the Pressure Field in a Turbulent Boundary Layer.* The Journal of the Acoustical Society of America, 1967. 42(2): p. 494-501.

[11] Maidanik, G., *Flush-Mounted Pressure Transducer Systems as Spatial and Spectral Filters.* The Journal of the Acoustical Society of America, 1967. 42(5): p. 1017-1024.

[12] Blake, W. and D.M. Chase, *Wavenumber-Frequency Spectra of Turbulent-Boundary-Layer Pressure Fluctuations Measured by Microphone Arrays*. 1969, Bolt, Beranek and Newman Inc.

[13] Blake, W.K. and D.M. Chase, *Wavenumber-Frequency Spectra of Turbulent-Boundary-Layer Pressure Measured by Microphone Arrays.* The Journal of the Acoustical Society of America, 1971. 49(3B): p. 862-877.

[14] Farabee, T.M. and F.E.J. Geib, *Measurements of Boundary Layer Pressure Fluctuations at Low Wavenumbers on Smooth and Rough Walls*, in *NCA - Flow Noise Modeling, Measurement, and Control*, T.M. Farabee, W.L. Keith, and R.M. Lueptow, Editors. 1991, ASME. p. 55-68.

[15] Kudashev, E.B., *Spatial filtering of wall pressure fluctuations beneath a turbulent boundary layer.* Acoustical Physics, 2007. 53(5): p. 629-637.

[16] Abraham, B.M. and W.L. Keith, *Direct Measurements of Turbulent Boundary Layer Wall Pressure Wavenumber-Frequency Spectra.* Journal of Fluids Engineering, 1998. 120(1): p. 29-39.

[17] Manoha, E., *The wavenumber-frequency spectrum of the wall pressure fluctuations beneath a turbulent boundary layer*, in *2nd AIAA/CEAS Aeroacoustics Conference*. 1996: State College, PA.

[18] Bremner, P., C. Todter, and S. Clifton, *Sideglass Turbulence and Wind Noise Sources Measured with a High Resolution Surface Pressure Array*. 2015, SAE International.

[19] Martin, N.C. and P. Leehey, *Low wavenumber wall pressure measurements using a rectangular membrane as a spatial filter.* Journal of Sound and Vibration, 1977. 52(1): p. 95-120.

[20] Bonness, W.K., D.E. Capone, and S.A. Hambric, *Low-wavenumber turbulent boundary layer wall-pressure measurements from vibration data on a cylinder in pipe flow.* Journal of Sound and Vibration, 2010. 329(20): p. 4166-4180.

[21] Golubev, A.Y., *Experimental estimate of wave spectra of wall pressure fluctuations of the turbulent boundary layer in the subconvective region.* Acoustical Physics, 2012. 58(4): p. 396-403.

[22] Maxit, L., *Simulation of the pressure field beneath a turbulent boundary layer using realizations of uncorrelated wall plane waves.* The Journal of the Acoustical Society of America, 2016. 140(2): p. 1268-1285.

[23] Arguillat, B., et al., *Measurements of the Wavenumber-Frequency Spectrum of Wall Pressure Fluctuations under Turbulent Flows*, in *11th AIAA/CEAS Aeroacoustics Conference*. 2005: Monterey, California.

[24] Arguillat, B., et al., *Measured wavenumber: Frequency spectrum associated with acoustic and aerodynamic wall pressure fluctuations.* The Journal of the Acoustical Society of America, 2010. 128(4): p. 1647-1655.

[25] Salze, E., et al., *An experimental characterisation of wall pressure wavevector-frequency spectra in the presence of pressure gradients*, in AIAA Aviation 14. 2014: Atlanta, GA.

[26] Salze, E., et al., *An experimental investigation of wall pressure fluctuations beneath pressure gradients*, in AIAA Aviation 2015. 2015: Dallas, TX.

[27] Prigent, S.L., et al., *Deconvolution of the wave number - frequency spectra of wall pressure fluctuations*, in AIAA Aviation 2018. 2018: Atlanta, GA.

[28] Prigent, S.L., É. Salze, and C. Bailly, *Deconvolution of Wave-Number-Frequency Spectra of Wall Pressure Fluctuations.* AIAA Journal, 2019. Articles in advance.

[29] Ehrenfried, K. and L. Koop, *Pressure Fluctuations Beneath a Compressible Turbulent Boundary Layer*, in 14th AIAA/CEAS Aeroacoustics Conference (29th AIAA Aeroacoustics Conference). 2008: Vancouver BC.

[30] Gabriel, C., et al., *Measurement of the spatial coherence of surface pressure in the wake of a car's side mirror*, in 19th AIAA/CEAS Aeroacoustics Conference. 2013: Berlin.

[31] Schram, C.F. and N. Van de Wyer, *An optimized microphone array for the measurement of turbulent boundary layer wall pressure wavenumber-frequency spectra*, in AIAA Aviation 2018. 2018: Atlanta, GA.

[32] Fritsch, D.J., et al., *The Pressure Signature of High Reynolds Number Smooth Wall Turbulent Boundary Layers in Pressure Gradient Family*, in AIAA Aviation Forum. 2020: Virtual.

[33] Fritsch, D., et al., *The Space-Time Correlation of Pressure Under High Reynolds Number Smooth Wall Turbulent Boundary Layers in Pressure Gradient Family*, in AIAA Scitech 2021 Forum. 2021: Virtual.

[34] Duetsch-Patel, J. E., Vishwanathan, V., Minionis, J. B., Totten, E., Gargiulo, A., Fritsch, D. J., Szoke, M., Borgoltz, A., Roy, C. J., Lowe, K. T., et al., *Aerodynamic Design and Assessment of Modular Test Section Walls for CFD Validation in Hybrid Anechoic Wind Tunnels*, AIAA Scitech 2020 Forum, 2020, p. 2214.

[35] Clauser, F., *The Turbulent Boundary Layer*, Advanced Applied Mechanics, 1956, 4: pp. 1-54

[36] Spalding, D.B., *A Procedure for the Calculation of Boundary Layers Confined in Ducts*, Journal of Engineering Physics, 1970, Vol. 19, pp. 1085-1090

[37] Damani, S., Alexander, W. N., Devenport, W. J., Pearce, B. P., Shelley, S. R., Starkey, T. A., Hibbins, A. P., and Sambles, J. R. *Excitation of Airborne Acoustic Surface Modes Driven by a Turbulent Flow*, AIAA Journal. Aug 2021.

[38] Damani. S., *Excitation of Acoustic Surface Waves by Turbulence (Master's thesis)*, VTechWorks, July 2021.

[39] DeGraaff, D. B., Eaton, J. K., *Reynolds-number scaling of the flat-plate turbulent boundary layer*, J. Fluid Mech. (2000), vol. 422, pp. 319-346.